PCCP

PAPER

View Article Online
View Journal | View Issue

Check for updates

Cite this: *Phys. Chem. Chem. Phys.*, 2018, **20**, 11976

Comparing ammonia diffusion in NH_3-SCR zeolite catalysts: a quasielastic neutron scattering and molecular dynamics simulation study

A. J. O'Malley, *[ab] M. Sarwar,[c] J. Armstrong,[d] C. R. A. Catlow,[abe] I. P. Silverwood,[bd] A. P. E. York[c] and I. Hitchcock*[c]

The diffusion of ammonia in the small pore zeolite and potential commercial NH_3-SCR catalyst levynite (LEV) was measured and compared with its mobility in the chabazite (CHA) topology (more established in NO_x abatement catalysis), using quasielastic neutron scattering (QENS) and molecular dynamics (MD) simulations at 273, 323 and 373 K. The QENS experiments suggest that mobility in LEV is dominated by jump diffusion through the 8-ring windows between cages (as previously observed in CHA) which takes place at very similar rates in the two zeolites, yielding similar experimental self-diffusion coefficients (D_s). After confirming that the same characteristic motions are observed between the MD simulations and the QENS experiments on the picosecond scale, the simulations suggest that on the nanoscale, the diffusivity is higher by a factor of ~2 in the CHA framework than in LEV. This difference between zeolites is primarily explained by the CHA cages having six 8-ring windows in the building unit, compared to only three such windows in the LEV cage building unit, thereby doubling the geometric opportunities to perform jump diffusion between cages (as characterised by the QENS experiments) leading to the corresponding increase in the MD calculated D_s. The techniques illustrate the importance of probing both pico- and nanoscale dynamics when studying intracrystalline diffusion in both NH_3-SCR catalyst design, and in porous materials generally, where notable consistencies and differences may be found on either scale.

Received 13th February 2018,
Accepted 28th March 2018

DOI: 10.1039/c8cp01022f

rsc.li/pccp

Open Access Article. Published on 29 March 2018. Downloaded on 2/7/2026 3:26:43 AM.
This article is licensed under a Creative Commons Attribution 3.0 Unported Licence.

1. Introduction

The catalytic reduction of NO_x compounds is a well-established NO_x abatement technology in combustion engines, where the selective catalytic reduction with ammonia (NH_3-SCR) process in small pore metal exchanged zeolites is currently the leading technology for reducing emissions from oxygen rich diesel engines.[1–3]

Metal exchanged chabazite (CHA) zeolites such as Cu-SSZ-13 exhibit very high N_2 selectivity and are highly thermally stable, so are more suited to the harsh vehicle environments when compared to, for example, zeolites ZSM-5 and Beta;[4] hence their development in industry for NO_x abatement in diesel powered vehicles.[5–7] The CHA structure pores are 3.8 Å in diameter built from eight-membered rings,[8] and Cu-SSZ-13 in particular has high thermal stability, good N_2 selectivity, low N_2O formation and high hydrocarbon tolerance. The high thermal stability was attributed to the density of the framework structure, and also originally to the cation location just outside the six-membered rings.[9,10] However, it has been shown that on adsorption and interaction with gases, the ion is then pulled into the chabazite cages with an increase in its mobility.[11] Optimising NO_x abatement catalyst formulation and performance involves an understanding of the active site, mechanism and the reaction kinetics, and also of the diffusion of molecules in the porous catalyst structure.

While the CHA structure is by far the most studied of the 8-ring zeolite topologies for NH_3-SCR, other 8-ring structures such as levynite (LEV) and DDR zeolites[12] are also of interest, illustrated by recent patents on levyne zeolites for this application.[13,14] The LEV topology has the 8-rings in a 2-dimensional arrangement, compared to the 3-dimensional arrangement of CHA zeolites. It is therefore expected that characteristics such as active species mobility (crucial in catalyst design and optimisation) would be affected by this

[a] *Cardiff Catalysis Institute, School of Chemistry, Cardiff University, Main Building, Park Place, Cardiff, CF10 3AT, UK. E-mail: omalleya@cardiff.ac.uk*
[b] *UK Catalysis Hub, Research Complex at Harwell, Rutherford Appleton Laboratory, Harwell Oxford, Didcot, Oxfordshire OX11 0FA, UK*
[c] *Johnson Matthey Technology Centre, Blounts Court, Sonning Common, Reading RG4 9NH, UK. E-mail: iain.hitchcock@matthey.com*
[d] *ISIS Facility, STFC Rutherford Appleton Laboratory, Didcot, Oxon OX11 0QX, UK*
[e] *University College London, Department of Chemistry, Materials Chemistry, Third Floor, Kathleen Lonsdale Building, Gower Street, London WC1E 6BT, UK*

This journal is © the Owner Societies 2018

Open Access Article. Published on 29 March 2018. Downloaded on 2/7/2026 3:26:43 AM.
This article is licensed under a Creative Commons Attribution 3.0 Unported Licence.

difference in framework dimensionality. Indeed, the lower NO_x conversion after hydrothermal treatment in 2-dimensional small pore zeolites is considered to be due to a combination of sorbate diffusion constraints and lower Cu loading achieved through ion exchange.[12]

While the interaction of the ammonia reductant with the active sites in CHA catalysts has been studied,[11,15–18] microscopic diffusive behaviour in these systems had not been investigated until our recent measurements of NH_3 diffusion in commercially available H-CHA and Cu-CHA zeolite catalysts using quasielastic neutron scattering (QENS) and molecular dynamics (MD) simulations.[19] Indeed, neutron spectroscopic techniques are a growing tool in catalytic science[20] and may reveal much about molecule/active site interactions as illustrated by the significant insight obtained into the nanoscale behaviour of ammonia, and its mobility in CHA catalysts as a function of Cu^{2+} counterion presence. The experiment suggested the presence of Cu^{2+} had no effect on NH_3 mobility on the timescale of the experiment, which was explained through simulation, *via* the observation of clustering of the NH_3 around the counterion, shielding other NH_3 molecules from any interaction and thus allowing their unimpeded intercage movement. A similar phenomenon was previously observed for ammonia in silicalite using QENS and PFG-NMR, where an increase in diffusivity was observed with loading due to the blocking of silanol defect adsorption sites, allowing the overall mobility to rise.[21]

To our knowledge, there are no studies of the nanoscale mobility of active SCR species in other potential catalysts based on small pore zeolites. The combined use of QENS and MD simulations has proved to be very elucidative in studying dynamical behaviour in a number of zeolite systems,[22–28] particularly as more accurate contemporary classical models of the framework and sorbates are now able to calculate diffusion coefficients and activation energies which are much closer to experiment.[29,30] Given the detailed insight our combined QENS and MD studies gave into both the mobility, and the sorbate-framework interactions of reactive species in chabazite, we have used this combination of techniques to study NH_3 mobility in small pore zeolite levynite (LEV), where recent patents[13,14] indicate the commercial interest in pursuing other small pore topologies for NH_3-SCR catalysis. As noted, LEV contains 8-ring channels similar to CHA, but the channel system has a 2-dimensional topology compared to the 3-dimensional CHA topology. We therefore use this powerful combination of QENS and MD to probe potential diffusivity differences on the pico- and nano time scales between LEV and the more established CHA NH_3-SCR catalyst. We find that on a local, molecular scale, the mobility behaviour is very similar between the CHA and LEV topologies. On the nanoscale, however, the different framework structure has a marked effect on the overall diffusivity of NH_3.

2. Experimental

The material studied in this work was a commercially available H-LEV zeolite provided by Johnson Matthey, Si/Al = 34. Samples were in powder form and microporous only, as determined by nitrogen gas adsorption at 77 K.

2.1 QENS experiments

The H-LEV samples were placed in a stainless steel can and heated to 300 °C overnight at vacuum to remove any pre-adsorbed water. After cooling, the can was transferred to a glovebox under an argon atmosphere. The dry sample (4.1 grams in total) was transferred to a thin walled aluminium container of annular geometry. The aluminium cell was then connected to a gas inlet system, which allowed ammonia to be adsorbed onto the zeolite. The cell pressure was raised to 800 mbar to ensure the zeolite was saturated with ammonia, in order to directly compare with our previous CHA experiments in terms of loading.

All measurements were performed using the time-of-flight backscattering neutron spectrometer OSIRIS[31] at the ISIS Pulsed Neutron and Muon Source, Rutherford Appleton Laboratory, Oxfordshire. Pyrolytic graphite 002 analyser crystals were used to give an energy resolution of 24.5 μeV at full width at half maximum with energy transfers measured in a window of $\pm$0.55 meV; the detectors covered measurements over a Q range of 0.2–1.7 $Å^{-1}$. The measurement was taken of an empty zeolite sample and the signal was then subtracted from the signal of the loaded zeolite, so that only the signal from the ammonia could be extracted. In this way any scattering from the aluminium container, which is very low in comparison with the empty zeolite is also subtracted. No further corrections were necessary.

The QENS experiments were performed at 273, 323 and 373 K. The elastic resolution function was measured with a vanadium foil sample. All data were analysed using a combination of Mantid[32] and DAVE softwares.[33] A detailed discussion of the QENS method and its applicability to deriving dynamical characteristics of sorbates in zeolites can be found in the following ref. 24 and 34.

2.2 Molecular dynamics simulations

Molecular dynamics simulations were performed using Forcite as implemented in Materials Studio 8.0.[35] The simulations were run at 273 K, 323 K and 373 K to provide direct comparison with the QENS measurements. The coordinates of the LEV structure were obtained from the IZA database.[36] A 2 × 2 × 1 supercell containing 648 atoms with optimised lattice parameters of 26.47 × 26.45 × 22.65 Å was created and periodic boundary conditions were used. The Si atoms in the 8-rings were randomly substituted with Al atoms to give a Si/Al ratio of 17, consistent with our MD simulations of CHA in ref. 19. Charge compensation was achieved by adding protons to the O atoms adjacent to the Al atoms, with the acidic protons oriented pointing into the 8-ring of the LEV cage. Before the simulation, the NH_3 molecules and framework structures were optimised using the COMPASS force field[37] which represented the intra- and intermolecular forces throughout.

In order to provide a direct comparison with our previous study of NH_3 mobility in CHA, a loading of 90 NH_3 molecules were loaded into the supercell using a Monte Carlo docking algorithm as implemented in the Sorption module in Materials Studio.[35]

Open Access Article. Published on 29 March 2018. Downloaded on 2/7/2026 3:26:43 AM.
This article is licensed under a Creative Commons Attribution 3.0 Unported Licence.

These structures were then re-optimised and subjected to a simulated annealing procedure to ensure a low energy starting structure. Periodic boundary conditions were used throughout and the electrostatic interactions were calculated using an Ewald summation with an 11 Å cut-off; The zeolite framework was fully flexible in the simulations. The system was then equilibrated for 200 ps using a 1 fs time step, after which no statistically meaningful variation in energy was observed. Production runs were then started from these equilibrated systems and run for 5 ns, again using a timestep of 1 fs. The *NVT* ensemble, with a Nosé thermostat, was used throughout. The trajectory of the N atom was recorded every 250 steps during the course of the simulation. The calculations were run on a Dell Optiplex 7010 parallelised over 4 processors at Johnson Matthey Technology Centre, UK.

The mean squared displacements (MSD) obtained were evaluated for each temperature *via* the standard equation:

$$\mathrm{MSD}(t) = \frac{1}{N}\sum_{j=1}^{N}\left[\mathbf{r}_j(t_0 + t) - \mathbf{r}_j(t_0)\right]^2$$

where N corresponds to the number of NH_3 molecules and $\mathbf{r}_j(t_0)$ and $\mathbf{r}_j(t)$ to the initial and final positions of the molecular centre of mass over time interval t. The displacement may be calculated and averaged over many equal time intervals, the origin of which may be varied over the total trajectory in order to improve statistics, and calculate the standard error in the final D_s value. We calculated the error in the D_s after separating the total 5 ns MSD into 10 sections of 500 ps each.

The diffusion coefficients were obtained by fitting the MSD against time in the region 0–500 ps and assuming the Einstein relation below, (where the variation of log MSD *vs.* $\log t$ has a slope of 1 indicating diffusive behaviour):

$$\mathrm{MSD}(t) = A + 6Dt$$

Activation energies for self-diffusion were then obtained from an Arrhenius plot.

In our previous study of NH_3 mobility in chabazite (ref. 19), the MD simulations were equilibrated for 200 ps production run of 1 ns. To enable direct comparison of ammonia mobility between the CHA and LEV frameworks, the simulations were run again for 5 ns in CHA using the parameters outlined in ref. 19, and subjected to the same analysis outlined in the above paragraphs.

The trajectories of the MD simulations were used to calculate the dynamic structure factor $S(Q,\omega)$ of the NH_3 protons using the MDANSE program[38] using a discrete spherical Q grid ranging from 0.3 to 1.7 $Å^{-1}$ with bin widths of 0.1 $Å^{-1}$. A fitted Gaussian of width 24.5 μeV was used as the instrumental resolution function, and was convoluted with the $S(Q,\omega)$ to allow a direct comparison between simulation and experiment.

3. Results and discussion

3.1 Quasielastic neutron scattering experiments

The QENS spectra at Q = 1.01 $Å^{-1}$ (273, 323 and 373 K) are shown in Fig. 1. The spectra were fitted with the instrumental resolution function, a flat background and a single Lorentzian function suggesting one observable mode of motion on the instrumental timescale. The error in the neutron data points in Fig. 1 are assigned based on Poisson statistics.

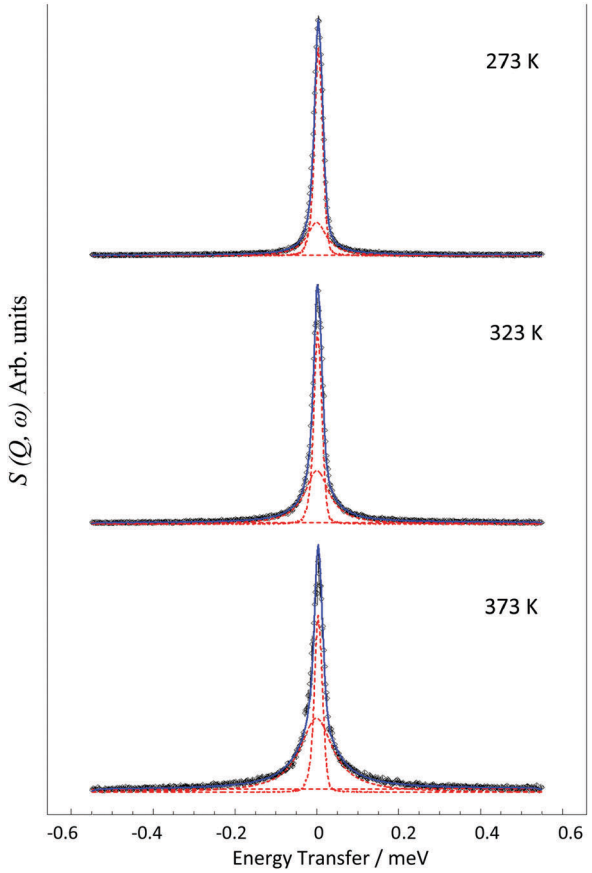

Fig. 1 QENS spectra obtained for ammonia diffusing in H-LEV at 273, 323 and 373 K at Q = 1.01 Å. (—) is the total fit, and (--) is used to represent the constituent resolution, Lorentzian and flat background functions.

We note that there is a significant elastic component in the spectra at all temperatures, which may typically be attributable to either a localised motion such as NH_3 rotation, or translational diffusion with a component of NH_3 which is static on the timescale sampled by the instrument. We characterise this component using the elastic incoherent structure factor (EISF) which is plotted for each temperature in Fig. 2. We note first that there is a significant dependence of the EISF with temperature suggesting the presence of an activated process over this temperature range.

The experimental EISF was then compared with the theoretical models for the EISF which may apply to NH_3 in LEV. These include rotational models such as jump rotation around 3 equivalent sites on a circle with a radius (r) approximately that of the N–H bond (1 Å), the theoretical EISF given by

$$A_0(Q) = \frac{1}{3}\left[1 + 2j_0\left(Qr\sqrt{3}\right)\right],$$

Open Access Article. Published on 29 March 2018. Downloaded on 2/7/2026 3:26:43 AM.
This article is licensed under a Creative Commons Attribution 3.0 Unported Licence.

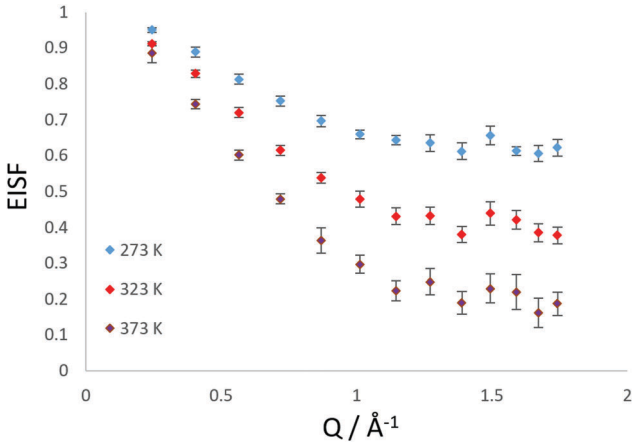

Fig. 2 Experimental EISF plots obtained at different temperatures for NH_3 in LEV.

where j_0 is the zero order spherical Bessel function. Isotropic rotation around a sphere of the same radius was also considered, with the theoretical EISF is given by

$$A_0(Q) = j_0^2(Qr).$$

We may also consider the model of diffusion confined to a spherical volume of radius r_{conf} as proposed by Volino and Dianoux,[39] where the theoretical EISF is given by

$$A_0(Q) = \left[\frac{3j_1(Qr_{conf})}{Qr_{conf}}\right]^2$$

where j_1 is the first order spherical Bessel function. Information on the models used to characterise such motions can be found in ref. 24 and 34 and detailed derivations of such models can also be found.[40]

As shown in Fig. 3, the rotational models appear to be a poor fit to the EISF, with the points laying above the experimental points at lower Q for all temperatures and below the experimental points at higher Q values at 273 and 323 K. The model for diffusion confined to a sphere of r = 3.5 Å exhibits the best matching shape to the experimental points, however falls below the experimental points at all Q values (apart from at Q = 0.28 for the highest temperature).

We have also considered that there may be a component of rotating NH_3 combined with a component undergoing translational diffusion confined to a sphere. Plots of the experimental EISF with the most optimal convolution of diffusion confined to a sphere with the 3-site jump rotation model are shown in Fig. 4. At 273 K and 323, the combinations do not replicate the shape of the EISF, falling above the experimental points at lower Q and below at higher Q. However, the shape of the experimental EISF is close to the theoretical model at 373 K with a rotational component weighted at 0.3.

Our best fits at all temperatures however, are obtained upon using the model of confined diffusion in a sphere with a component which is considered static on the timescale sampled by the instrument (~2–50 ps). We find the best fits were obtained with a spherical radius of 3.5 Å, and a mobile fraction of 0.37 at 273 K, 0.6 at 323 K and 0.8 at 373 K as shown in Fig. 5.

While our EISF analysis allows us to discount a significant contribution of rotational motions at 273 and 323 K, the possibility of such a contribution at 373 K must be addressed due to the EISF fitting in Fig. 4. In order to decipher which model at 373 K is correct between the confined diffusion/static component model, and the confined diffusion/rotational component model, we may use the dipole correlation function obtained from the MD simulations which allow us to assess whether the rotational relaxation time of the NH_3 protons around the centre of mass is within the window observable on the QENS instrument. We use the same method as described in a recent study of propane dynamics in porous TiO_2 [41] where the orientational-evolution of a unit vector along the N–H bonds are followed along another fixed vector in the molecular frame.

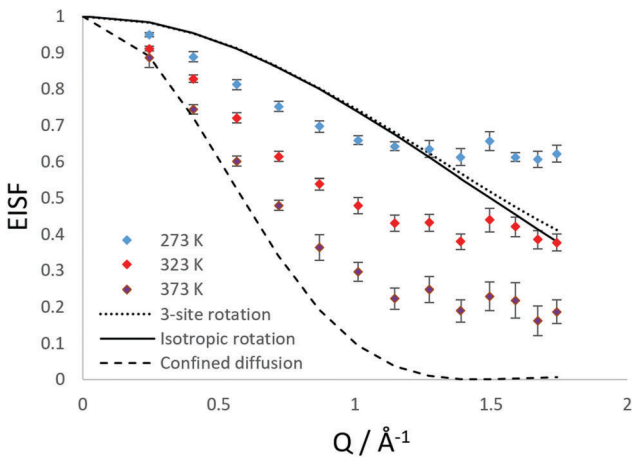

Fig. 3 Experimental EISF plots obtained at different temperatures for NH_3 in LEV, combined with theoretical models obtained from isotropic rotation, 3-site rotation around a circle (r = 1 Å) and diffusion confined to a sphere of radius 3.5 Å.

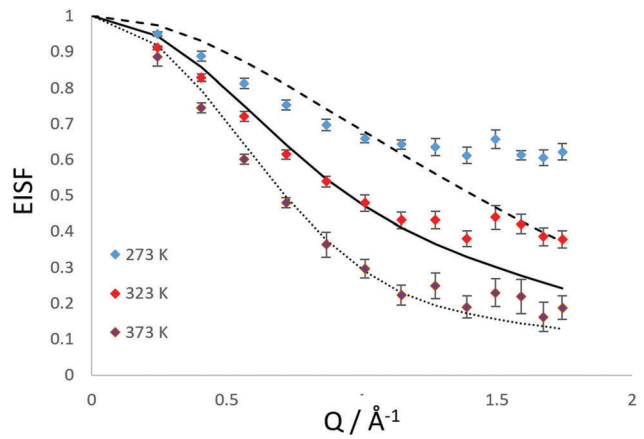

Fig. 4 Experimental EISF plots obtained at different temperatures for NH_3 in LEV, combining models of diffusion confined to a spherical volume of 3.5 Å, with a fraction rotating molecules set at 0.9 (- -), 0.57 (—) and 0.3 (· · ·).

Open Access Article. Published on 29 March 2018. Downloaded on 2/7/2026 3:26:43 AM.
This article is licensed under a Creative Commons Attribution 3.0 Unported Licence.

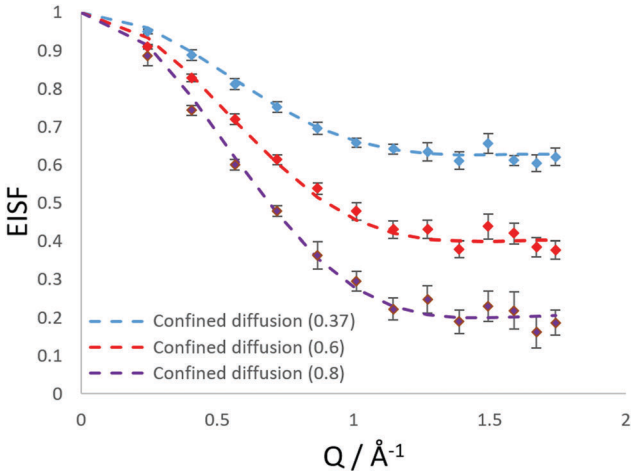

Fig. 5 Experimental EISF plots obtained at different temperatures for NH_3 in LEV, compared with models of diffusion confined to a spherical volume of 3.5 Å, with a mobile fraction of 0.37 (--), 0.6 (--) and 0.8 (--).

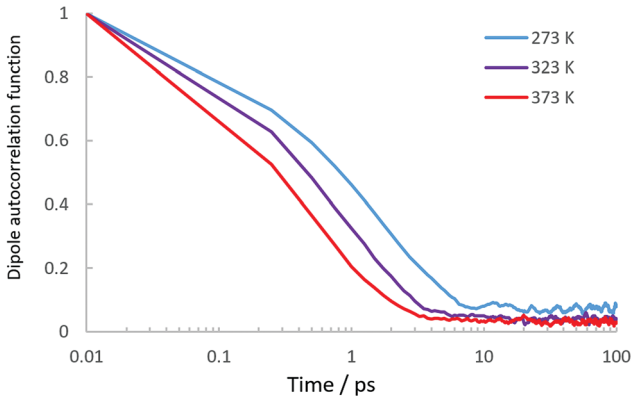

Fig. 6 Dipole autocorrelation functions calculated from our MD simulations of NH_3 in LEV.

The dipole correlation functions are plotted in Fig. 6. We note that the decay is very fast particularly at 373 K, and on the timescale observed by the QENS instrument would more likely produce a flat background, rather than a characterisable quasielastic component. To summarise, the EISF does not conform to a rotational model of ammonia, even when convoluted with confined translational motions (apart from potentially at 373 K), and the dipole correlation function suggests that the rotational relaxation is probably too fast to make a significant contribution to the spectra, especially at 373 K where the EISF may suggest such a rotational contribution. We can therefore conclude that the elastic contribution in our spectra is caused by molecules which are static on the timescale probed by OSIRIS, and that we are observing translational motions with an immobile fraction, rather than observing contributions from localised motions such as ammonia rotation. The presence of an immobile component which lowers with temperature may be related to the same observations as ammonia in silicalite[21] where strong binding to active sites was observed, needing thermal energy to break the strong non-bonded interactions.

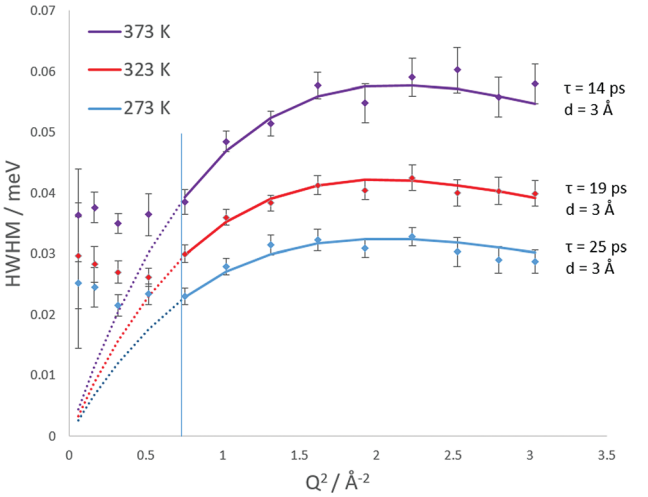

Fig. 7 Q dependencies of the HWHM of the quasielastic components of the QENS spectra at 273, 323 and 373 K. Each can be fit with a Chudley–Elliot jump diffusion model (solid and dotted coloured lines), the jump parameters are listed in each plot. The diffusion coefficient is also calculated using the Volino–Dianoux confined diffusion model from the low Q plateaued HWHM values as detailed in the text. The low Q widths used are illustrated by the dashed coloured lines, fitted using a least-squares method to the low Q data points.

The broadenings of the Lorentzian half-width at half-maximum (HWHM) are plotted at each temperature in Fig. 7. The errors in the Lorentzian HWHM are assigned using a Monte Carlo method where data sets are generated virtually within the neutron data point error bars and then fitted. We observe the plateauing of the HWHM below Q = 0.87 which conforms the Volino–Dianoux model of confined diffusion, where the Lorentzian width will plateau below $Q = \pi/r_{conf}$ where r_{conf} = 3.5 Å, consistent with the radius of LEV cages. After the plateauing region, we observed that at all temperatures the broadening fits to the Chudley and Elliot jump diffusion model,[42] with a fixed jump length of 3 Å.

We note that this is the same mode of motion as was detected in our previous study for ammonia diffusion in CHA.[19] The jump residence times decrease over the 273 K to 373 K range from 25–14 ps. The opportunity for jump diffusion arises from movement between LEV cages, as previously shown in CHA and illustrated later by our MD simulations. We therefore consider that the observed motion may be inter-spherical jumps between LEV cages (which are 3.5 Å in diameter) through the 8-ring windows, imposed by the LEV architecture.

The self-diffusion coefficients (D_s) were extrapolated using the Chudley–Elliot model as explained in ref. 23 and 33 and are listed in Table 1 (D_s (QENS, CE)). The coefficients measured are very close to, but slightly higher than those for the CHA system; however, the differences are within the error of the measurements. As with the CHA system, the measured diffusion coefficients are lower by a factor of 3 than those of ammonia obtained in silicalite[21] using QENS (with a pore diameter *ca.* 1.5 Å wider than levynite); though we note that our loadings are significantly higher than even the highest loading in that study (4.3 mol uc^{-1}). The diffusion coefficient may also be

Open Access Article. Published on 29 March 2018. Downloaded on 2/7/2026 3:26:43 AM.
This article is licensed under a Creative Commons Attribution 3.0 Unported Licence.

Table 1 Self-diffusion coefficients (D_s) in units of $m^2\ s^{-1}$ of ammonia in LEV and CHA at three different temperatures obtained from QENS experiments and MD simulations. Diffusion coefficients obtained from QENS experiments were derived using both the Chudley–Elliott jump diffusion model (QENS, CE), and the Volino–Dianoux confined diffusion model (QENS, VD) in LEV. D_s values measured in CHA by QENS are from our study in ref. 19

LEV					CHA		
T K	D_s (QENS, CE)	D_s (QENS, VD)	$D_{s\,nano}$ (MD)	$D_{s\,pico}$ (MD)	D_s (QENS, CE)	$D_{s\,nano}$ (MD)	$D_{s\,pico}$ (MD)
273	$6.63 \times 10^{-10} \pm 0.9 \times 10^{-10}$	$6.07 \times 10^{-10} \pm 0.57 \times 10^{-10}$	$1.06 \times 10^{-9} \pm 0.14 \times 10^{-9}$	2.4×10^{-9}	$6.0 \times 10^{-10} \pm 1.2 \times 10^{-10}$	$2.75 \times 10^{-9} \pm 0.72 \times 10^{-9}$	2.9×10^{-9}
323	$8.66 \times 10^{-10} \pm 1.3 \times 10^{-10}$	$8.1 \times 10^{-10} \pm 0.54 \times 10^{-10}$	$1.76 \times 10^{-9} \pm 0.3 \times 10^{-9}$		$7.6 \times 10^{-10} \pm 1.5 \times 10^{-10}$	$3.73 \times 10^{-9} \pm 0.45 \times 10^{-9}$	
373	$10.8 \times 10^{-10} \pm 1.5 \times 10^{-10}$	$10.2 \times 10^{-10} \pm 0.59 \times 10^{-10}$	$2.13 \times 10^{-9} \pm 0.44 \times 10^{-9}$		$9.4 \times 10^{-10} \pm 1.7 \times 10^{-10}$	$4.95 \times 10^{-9} \pm 0.33 \times 10^{-9}$	
E_a (kJ mol^{-1})	4.1	4.4	6.0		3.7	4.9	

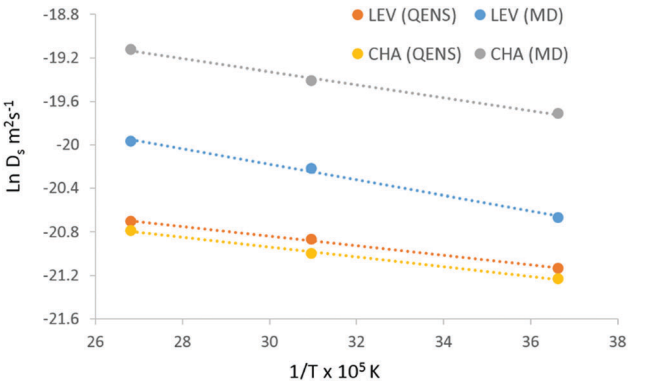

Fig. 8 Arrhenius plots for diffusion of ammonia in levynite and chabazite using QENS (D_s (QENS, CE)) and MD, the activation energies obtained are listed in Table 1.

estimated *via* the Volino–Dianoux model, where HWHM values at the low Q plateau at $(4.33D_s)/(r_{conf}^2)$. Using r_{conf} = 3.5 Å we obtain the D_S values listed in Table 1 (D_s (QENS, VD)) and note that they are similar within error of those obtained using the Chudley–Elliot jump diffusion model.

Crystallite size may also affect the measured diffusivity due to surface barrier effects if the crystallite is too small.[43] This effect is not significant in our experiment, as the Angström to nanometre length scale of movement probed by the QENS method is significantly less than the size of the zeolite crystals in our study (~1–2 μm).

The activation energies were calculated from the Arrhenius plot shown in Fig. 8 and are listed in Table 1. The experimental activation energy is slightly higher than that observed in chabazite by 0.4 kJ mol^{-1}, but we emphasise again the similarity between the extrapolated diffusion coefficients in both systems, which were within the error of the technique. In our previous study of ammonia in chabazite, we noted that over the timescale of the experiment, the dominant motion observed was the jump diffusion between chabazite cages through the 8-ring windows which separated them. The current QENS experiments suggest that the same movement is being observed, and that the change in dimensionality of the system affects neither the rate, nor dominance of this motion in the experimental observations.

3.2 Molecular dynamics simulations

For a direct comparison between the QENS measurements and MD simulations in both zeolite systems we may calculate the dynamic structure $S(Q,\omega)$ which is calculated from the molecular trajectories through

$$S(Q,\omega) = \frac{1}{\pi}\int I(Q,t)\exp(-i\omega t)\mathrm{d}t,$$

which is a discrete Fourier transform over a discrete Q and t range of the intermediate scattering function $I(Q,t)$, directly calculated from the molecular trajectories of the NH_3 protons

$$\langle I(Q,t)\rangle = \frac{1}{N}\sum_{i=1}^{N}\left\langle \frac{\sin(|Q||R(t+t_0)-R(t_0)|)}{|Q||R(t+t_0)-R(t_0)|}\right\rangle$$

Open Access Article. Published on 29 March 2018. Downloaded on 2/7/2026 3:26:43 AM.
This article is licensed under a Creative Commons Attribution 3.0 Unported Licence.

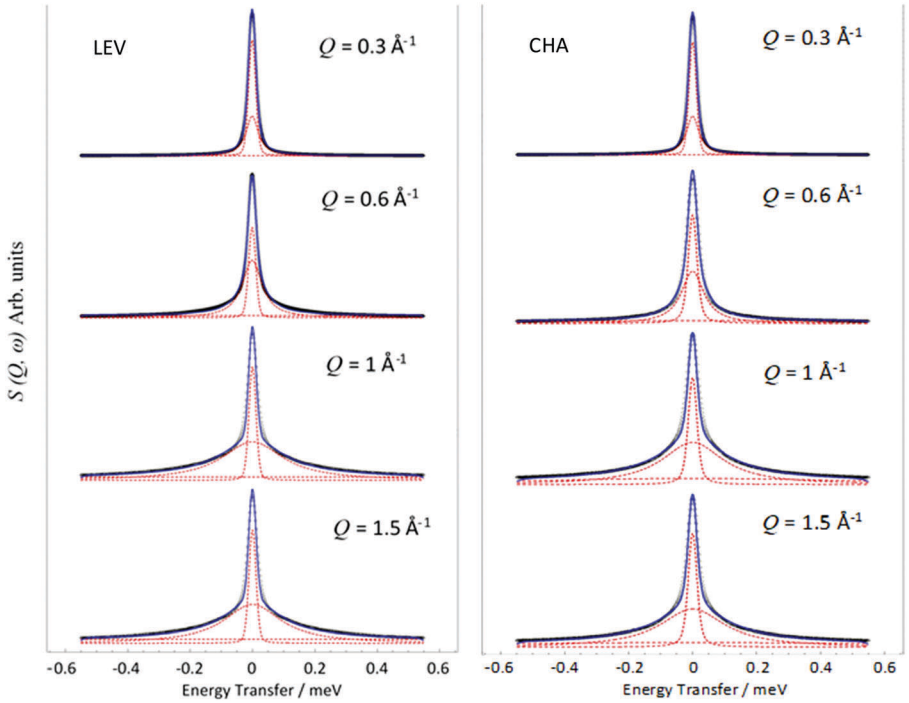

Fig. 9 $S(Q,\omega)$ obtained and fitted from MD simulations of ammonia in LEV (left) and CHA (right) at 273 K at a range of Q values. (--) is the total fit, and (--) represent the constituent resolution, Lorentzian and flat background functions.

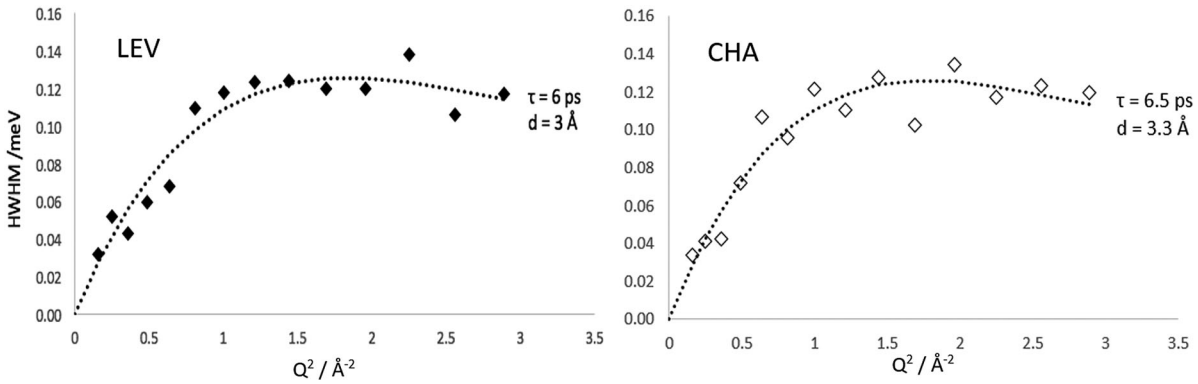

Fig. 10 Widths of the Lorentzian broadenings of $S(Q,\omega)$ calculated directly from MD simulations in LEV and CHA at 273 K.

where $R(t)$ and $R(t_0)$ are the position vectors of the NH_3 protons at time t and $t = 0$.

Examples of the $S(Q,\omega)$ calculated from the MD simulations are shown in Fig. 9. We note that these can also be fit with a single Lorentzian function as with the experimental data, the broadenings of which may be fitted to the appropriate model to derive the diffusivity in the time window probed by the QENS instrument ($\sim$2–50 ps).

The HWHM of the Lorentzian components fitted to the MD calculated $S(Q,\omega)$ in both zeolite systems are plotted in Fig. 10. In both LEV and CHA we observe a Q dependence which could be fitted to the Chudley–Elliot jump diffusion model with the same jump lengths as the experimental data. We note that the fitted residence time is significantly lower than that obtained experimentally at about 6 ps in LEV and 6.5 ps in CHA. The picoscale D_s values ($D_{s\,pico}$) calculated from these jump parameters are 2.4×10^{-9} m^2 s^{-1} in LEV and 2.9×10^{-9} m^2 s^{-1} in CHA (the larger $D_{s\,pico}$ in CHA despite the lower residence time is due to the slightly longer calculated jump distance) and are listed in Table 1. Potential reasons for this lower residence time in the MD compared to the QENS are considered when discussing the overall change in mobility in later paragraphs, pertaining to the generic forcefield use and perfect zeolite crystal. However, we can be confident in our further comparisons that the same type of motion is being observed between the experiment and our simulations. Crucially, we can also conclude that on the picoscale, the diffusivity of ammonia is very similar between LEV and CHA, taking place through jump diffusion which happens at similar rates.

Now that we are able to validate that the same mode of motion is observed on the picoscale in our simulations as in

Open Access Article. Published on 29 March 2018. Downloaded on 2/7/2026 3:26:43 AM.
This article is licensed under a Creative Commons Attribution 3.0 Unported Licence.

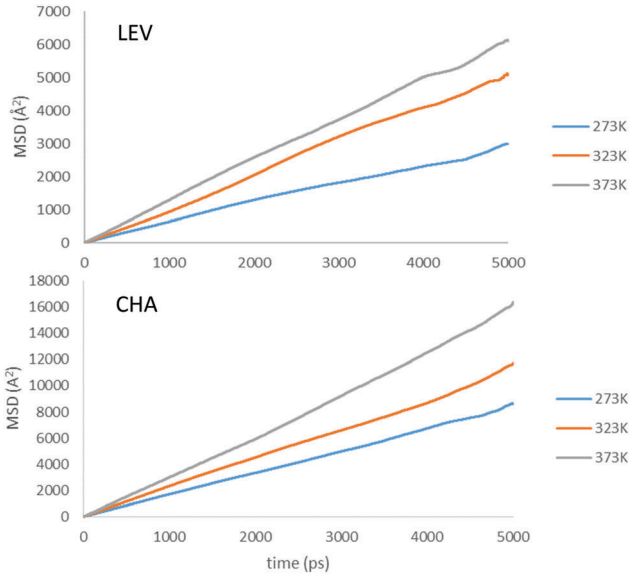

Fig. 11 Mean squared displacement (MSD) plots of NH_3 in H-LEV and H-CHA obtained from the MD simulations at 273, 323 and 373 K.

experiment, and that the rates of motion are very similar between both zeolites, we will now use the MD simulations to probe the nanoscale mobility of ammonia. Mean Squared Displacement (MSD) plots are presented in Fig. 11 in H-LEV along with those newly calculated for H-CHA at 273 K, 323 K and 373 K. They appear linear at all temperatures, indicating that the statistics in our simulations are sufficient for calculating accurate diffusion coefficients. The calculated diffusion coefficients of NH_3 in LEV and CHA are listed in Table 1 (termed $D_{s\,nano}$ MD) and are plotted in Fig. 12.

We note that the absolute values of D_s calculated from the MD simulations are roughly a factor of 2 higher than those measured by QENS in H-LEV, and a factor of 5 higher than those measured by QENS in H-CHA. The observation of higher calculated diffusivities than those from experiment is common in microscopic studies of sorbate diffusion in zeolites,[24,33] often attributed to the ideal zeolite crystal used in the simulation model. The experimental sample is likely to have defects,

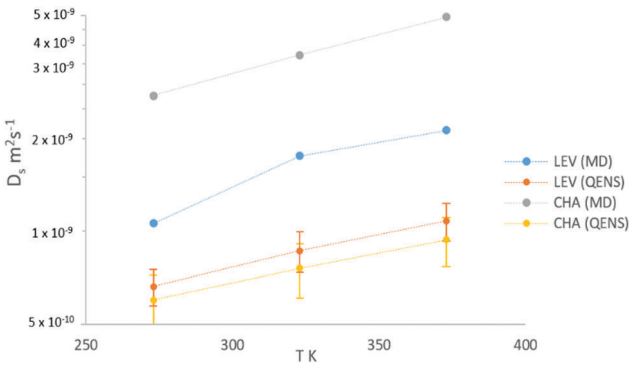

Fig. 12 Plot of self-diffusion coefficients of NH_3 in H-LEV from QENS and MD simulations ($D_{s\,nano}$), compared with those for the CHA system obtained by both by QENS and MD.

such as silanol nests and extra-framework aluminium which could hinder sorbate diffusion. An additional reason for the observed difference may be use of the COMPASS force field, which is a generic force field not developed and fitted for these specific systems. Despite the agreement achieved in this study it is important to recognise that any generic force field will have inherent approximations which can only be properly addressed through detailed empirical (or quantum mechanical) fitting of guest–host interactions.

In contrast to the QENS experiments, the MD simulations show a significant difference between the diffusivities calculated in H-CHA and H-LEV. The calculated $D_{s\,nano}$ values are lower in H-LEV than in H-CHA by a factor of 2.5, 2.1 and 2.3 at 273, 323 and 373 K respectively. To explain the difference between the calculated CHA and LEV diffusion coefficients we first consider the MSD plots in the individual directions as shown for 273 K in H-LEV and H-CHA in Fig. 13, where the level of diffusion anisotropy is shown. The 2 dimensional topology of the channels formed from the 8-ring openings in the LEV cage leads to an absence of diffusion in the 001 direction, the equivalent of which is available for diffusion in CHA. This feature is illustrated by the trajectory plot in Fig. 14 which shows the 2D nature of the diffusion in this topology due to the lack of mobility available through the single and double 6-ring windows in this direction. The trajectory plot also illustrates that molecular transport takes place through a jump diffusion mechanism through 8-ring cages as found in the QENS studies.

While the anisotropy is a contributing factor to the lower overall diffusivity, it is not however the principle reason for the nanoscale NH_3 diffusivity being over a factor of 2 lower in the LEV framework than in CHA. Upon examining the MSD in the individual directions in Fig. 13, we note that even in the mobile 100 and 010 directions, the MSD is significantly lower than that for CHA in Fig. 6. The difference suggests a significantly higher degree of mobility in CHA than in LEV even when the anisotropy is accounted for. An explanation is given upon examining the combined building units of both structures as shown in Fig. 15. The combined building unit of LEV (92 atoms) comprises of a levynite cage (*lev*) and a double 6-ring (*d6r*). The combined building unit of CHA (108 atoms) comprises of a chabazite cage (*cha*) and a double 6-ring (d6r). Despite only a slight increase in size (both in terms of the number of atoms and the volume), there are double the number of 8-rings through which NH_3 may diffuse in the CHA structure. Three of the 8-rings in the CHA structure are replaced by 6-rings (which do not allow transport through) in the LEV structure as illustrated in Fig. 8.

The increased opportunities to leave the cage in CHA are illustrated in Fig. 16, where we show that migration occurs through all the available 8-rings (six in the CHA structure, and three in the LEV structure), and the NH_3 molecule therefore has double the number of geometric opportunities to perform intercage diffusion in CHA, explaining its D_s increasing by a factor of $\sim$2 in the simulations between the two zeolites.

We consider again the QENS experiments and our MD simulations analysed at the picosecond scale, which in contrast

Open Access Article. Published on 29 March 2018. Downloaded on 2/7/2026 3:26:43 AM.
This article is licensed under a Creative Commons Attribution 3.0 Unported Licence.

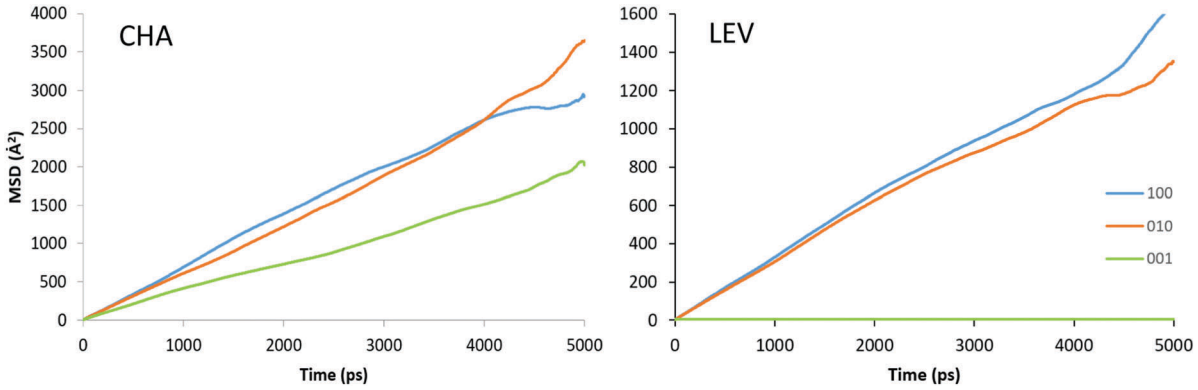

Fig. 13 MSD plots of NH_3 along the three principle axes of CHA and LEV at 273 K.

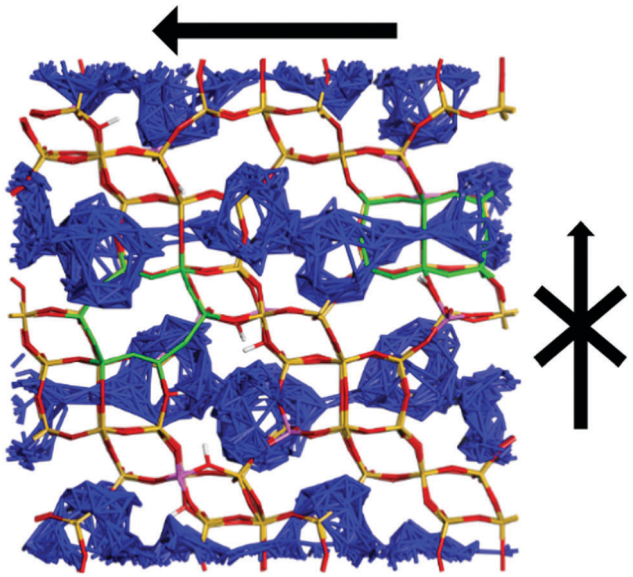

Fig. 14 Trajectory plots viewed from the 100 direction for diffusion of ammonia in levynite, at 273 K. The anisotropy is illustrated where no diffusion through the single or double 6-ring windows linking the cages (highlighted in green) is permitted, which are the only opportunities for intercage mobility in the 001 direction, or single 6-rings linking the LEV cages.

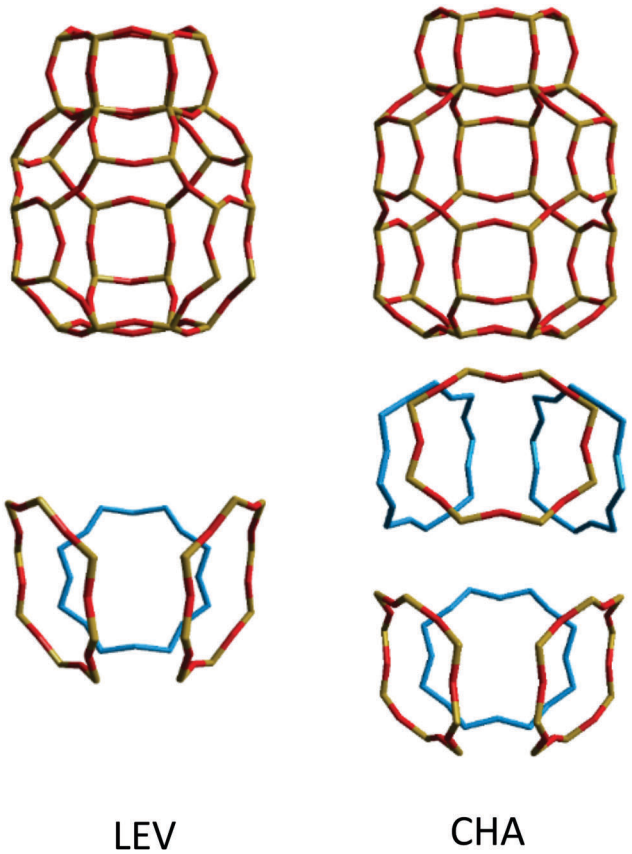

Fig. 15 (top) Combined building units for LEV and CHA, with the structural 8-rings highlighted and separated (bottom).

to the MD simulations analysed at the nanoscale suggested that the mobility was the same between the two zeolites, as the jump diffusion mechanism observed has the same residence times and jump length. We now consider that rather than contrasting with the MD simulations, the QENS is probing the mode of motion present in the simulations (the intercage jumps through 8-rings), which take place at the same rate in both zeolites; but does not show the frequency with which these jumps take place (which increases by a factor of ~ 2 in CHA, in conjunction with the number of 8-rings).

In showing that the intercage jump diffusion behaviour and rate is the same between the two zeolites using QENS and the MD simulations, but that the measured $D_{s\,nano}$ throughout the supercell in the MD simulations differs by a factor of 2, (due to increased opportunities to perform said intercage jumps), the two methods have revealed both consistencies in the behaviour of ammonia between the two zeolites on the local molecular scale, but also illustrated significant differences on the nanoscale, both of which are a direct consequence of the zeolite structure. Our observations not only show both important consistencies and inconsistencies in the dynamical behaviour of the reductant in potential NH_3-SCR catalysts, but demonstrate the importance of multiscale study in understanding sorbate behaviour in microporous catalyst design. The ability for combined experimental and theoretical studies to observe and explain such behaviour is also illustrated.

Open Access Article. Published on 29 March 2018. Downloaded on 2/7/2026 3:26:43 AM.
This article is licensed under a Creative Commons Attribution 3.0 Unported Licence.

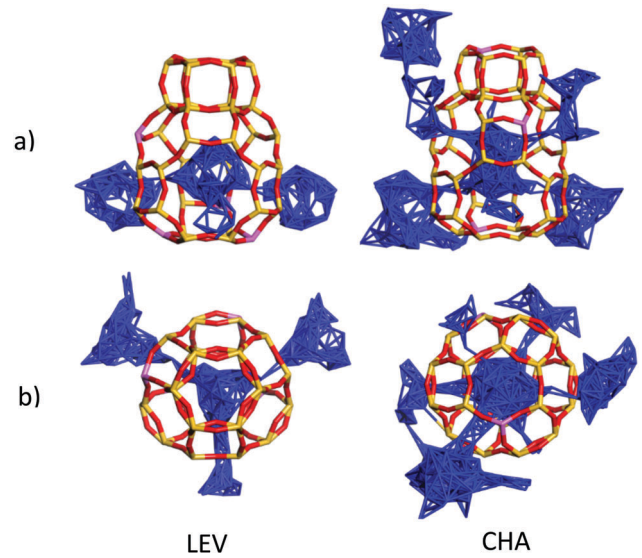

Fig. 16 Centre-of-mass trajectory plots of an NH_3 molecule during the MD simulations, viewed from (a) the side of a selected combined building unit and (b) above the combined building unit. We observe diffusion through the 3 available 8-rings in the LEV unit compared to diffusion though the 6 available 8-rings in the CHA unit. We note in both structures that no diffusion is observed through the double 6-ring (*d6r*) units.

4. Summary and conclusions

To understand the influence of framework topology on molecular diffusion in NH_3-SCR catalyst design, we have studied the diffusion of ammonia in commercial zeolite levynite (Si/Al = 34) using a combination of QENS and MD simulations between 273 and 373 K. Results were compared with our previous measurements in chabazite (with new MD simulations performed over the same time length in CHA) using the same techniques, to probe any differences in mobility between the 2D LEV structure and the 3D CHA structure. The QENS experiments observed translational diffusion confined to a sphere with a radius of $\sim$3.5 Å (consistent with the radius of LEV cages), exhibiting a jump diffusion mechanism with a fixed distance of 3 Å, consistent with inter-spherical jumps through the 8-ring windows which link the LEV cages together, as observed in our previous studies in CHA. The extrapolated D_s values were 6.6–10.8 $\times$ 10^{-10} m^2 s^{-1}, within error of those obtained in CHA at the same temperatures, suggesting that on the timescale probed by the QENS experiments, the ammonia mobility is the same between the two zeolites. Upon analysing the MD simulations on the picoscale, we observe that the same mode of motion is observed taking place at similar rates between the two frameworks. This consistency between LEV and CHA contrasted with the MD simulations when they were analysed on the nanoscale, which gave D_s values of 1–2.1 $\times$ 10^{-9} m^2 s^{-1} which in LEV were a factor of $\sim$2 lower than those obtained for NH_3 in CHA at the same temperatures. This difference in nanoscale mobility was attributed to the differing structures of the building units for each zeolite, where the levynite cage (*lev*) building unit contains three 8-ring windows compared to the six 8-ring windows in the chabazite cage (*cha*) building unit. The doubling in geometric opportunities for ammonia to jump between chabazite cages through these windows, observed by the QENS experiments, is consistent with the increase in $D_{s\,nano}$ by a factor of $\sim$2. Our observations that the diffusion coefficients between the two zeolites are measured within error of each other using QENS (and also very similar in the picoscale analysis of the MD simulations), but a factor of $\sim$2 different from the nanoscale analysis of the MD simulations illustrates the importance of measuring over different time and length scales in such systems. The local molecular scale probed by our QENS experiments (jump diffusion through 8-ring windows) showed significant similarities in ammonia mobility between the two zeolites, compared to the larger nanoscale probed by our MD simulations which show significant differences, directly caused by the difference in zeolite catalyst topology. Data underpinning the results presented here can be found at DOI: 10.5286/ISIS.E.63530347.

Conflicts of interest

There are no conflicts to declare.

Acknowledgements

We acknowledge Johnson Matthey for both the provision of samples and for the permission to study their materials in this publication. The authors acknowledge the ISIS Pulsed Neutron and Muon Source for access to beamline facilities (Experiment RB: 1520464), and the assistance of Dr Stewart Parker during the experimental stage and following discussions. AJOM would like to acknowledge the Ramsay Trust for provision of the Ramsay Trust Memorial Fellowship. We acknowledge the Engineering and Physical Sciences Research Council (EPSRC): grant no. EP/G036675/1 for financial support under their Centres for Doctoral Training scheme and the Science and Technologies Facilities Council. Prof. Nora De Leeuw is thanked for funding under the EPSRC grant EP/K009567/2. The UK Catalysis Hub is kindly thanked for resources and support provided *via* our membership of the UK Catalysis Hub Consortium and funded by EPSRC (grants EP/K014706/1, EP/K014668/1, EP/K014854/1EP/K014714/1 and EP/M013219/1).

References

1 R. M. Heck, R. J. Farrauto and S. T. Gulati, *Catalytic air pollution control: commercial technology*, John Wiley & Sons, 2009.
2 S. Brandenberger, O. Kröcher, A. Tissler and R. Althoff, *Catal. Rev.*, 2008, **50**, 492–531.
3 A. M. Beale, F. Gao, I. Lezcano-Gonzalez, C. H. Peden and J. Szanyi, *Chem. Soc. Rev.*, 2015, **44**, 7371–7405.
4 J. H. Kwak, R. G. Tonkyn, D. H. Kim, J. Szanyi and C. H. Peden, *J. Catal.*, 2010, **275**, 187–190.

Open Access Article. Published on 29 March 2018. Downloaded on 2/7/2026 3:26:43 AM. This article is licensed under a Creative Commons Attribution 3.0 Unported Licence.

5 I. Bull, A. Moini, G. S. Koermer, J. A. Patchett, W. M. Jaglowski and S. Roth, *US Pat.*, 7704475, 2010.
6 I. Bull, W.-M. Xue, P. Burk, R. S. Boorse, W. M. Jaglowski, G. S. Koermer, A. Moini, J. A. Patchett, J. C. Dettling and M. T. Caudle, *US Pat.*, 7601662, 2009.
7 I. Bull, W.-M. Xue, P. Burk, R. S. Boorse, W. M. Jaglowski, G. S. Koermer, A. Moini, J. A. Patchett, J. C. Dettling and M. T. Caudle, *US Pat.*, 8735311, 2014.
8 S. I. Zones, *US Pat.*, 4544538, 1985.
9 D. W. Fickel and R. F. Lobo, *J. Phys. Chem. C*, 2009, **114**, 1633–1640.
10 S. T. Korhonen, D. W. Fickel, R. F. Lobo, B. M. Weckhuysen and A. M. Beale, *Chem. Commun.*, 2011, **47**, 800–802.
11 U. Deka, A. l. Juhin, E. A. Eilertsen, H. Emerich, M. A. Green, S. T. Korhonen, B. M. Weckhuysen and A. M. Beale, *J. Phys. Chem. C*, 2012, **116**, 4809–4818.
12 D. W. Fickel, E. D'Addio, J. A. Lauterbach and R. F. Lobo, *Appl. Catal., B*, 2011, **102**, 441–448.
13 I. Bull, U. Müller and B. Yilmaz, *US Pat.*, 20160129431, 2015.
14 I. Bull, U. Müller and B. Yilmaz, *US Pat.*, 9242241, 2016.
15 I. Lezcano-Gonzalez, U. Deka, B. Arstad, A. Van Yperen-De Deyne, K. Hemelsoet, M. Waroquier, V. Van Speybroeck, B. M. Weckhuysen and A. M. Beale, *Phys. Chem. Chem. Phys.*, 2014, **16**, 1639–1650.
16 I. Lezcano-Gonzalez, D. S. Wragg, W. A. Slawinski, K. Hemelsoet, A. Van Yperen-De Deyne, M. Waroquier, V. Van Speybroeck and A. M. Beale, *J. Phys. Chem. C*, 2015, **119**, 24393–24403.
17 F. Giordanino, E. Borfecchia, K. A. Lomachenko, A. Lazzarini, G. Agostini, E. Gallo, A. V. Soldatov, P. Beato, S. Bordiga and C. Lamberti, *J. Phys. Chem. Lett.*, 2014, **5**, 1552–1559.
18 K. A. Lomachenko, E. Borfecchia, C. Negri, G. Berlier, C. Lamberti, P. Beato, H. Falsig and S. Bordiga, *J. Am. Chem. Soc.*, 2016, **138**, 12025–12028.
19 A. J. O'Malley, I. Hitchcock, M. Sarwar, I. P. Silverwood, S. Hindocha, C. R. A. Catlow, A. P. E. York and P. Collier, *Phys. Chem. Chem. Phys.*, 2016, **18**, 17159–17168.
20 A. J. O'Malley, S. F. Parker and C. R. A. Catlow, *Chem. Commun.*, 2017, **53**, 12164–12176.
21 H. Jobic, H. Ernst, W. Heink, J. Kärger, A. Tuel and M. Bée, *Microporous Mesoporous Mater.*, 1998, **26**, 67–75.
22 A. J. O'Malley, V. G. Sakai, I. P. Silverwood, N. Dimitratos, S. F. Parker and C. R. A. Catlow, *Phys. Chem. Chem. Phys.*, 2016, **18**, 17294–17302.
23 L. N. Gergidis, D. N. Theodorou and H. Jobic, *J. Phys. Chem. B*, 2000, **104**, 5541–5552.
24 H. Jobic and D. N. Theodorou, *Microporous Mesoporous Mater.*, 2007, **102**, 21–50.
25 A. J. O'Malley, C. R. A. Catlow, M. Monkenbusch and H. Jobic, *J. Phys. Chem. C*, 2015, **119**, 26999–27006.
26 V. Sharma, S. Gautam, S. Mitra, M. N. Rao, A. Tripathi, S. Chaplot and R. Mukhopadhyay, *J. Phys. Chem. B*, 2009, **113**, 8066–8072.
27 A. Sayeed, S. Mitra, A. Anil Kumar, R. Mukhopadhyay, S. Yashonath and S. Chaplot, *J. Phys. Chem. B*, 2003, **107**, 527–533.
28 R. Mukhopadhyay, A. Sayeed, S. Mitra, A. A. Kumar, M. N. Rao, S. Yashonath and S. Chaplot, *Phys. Rev. E: Stat., Nonlinear, Soft Matter Phys.*, 2002, **66**, 061201.
29 A. J. O'Malley and C. R. A. Catlow, *Phys. Chem. Chem. Phys.*, 2013, **15**, 19024–19030.
30 A. J. O'Malley and C. R. A. Catlow, *Phys. Chem. Chem. Phys.*, 2015, **17**, 1943–1948.
31 M. T. Telling and K. H. Andersen, *Phys. Chem. Chem. Phys.*, 2005, **7**, 1255–1261.
32 O. Arnold, J.-C. Bilheux, J. Borreguero, A. Buts, S. I. Campbell, L. Chapon, M. Doucet, N. Draper, R. F. Leal and M. Gigg, *Nucl. Instrum. Methods Phys. Res., Sect. A*, 2014, **764**, 156–166.
33 R. T. Azuah, L. R. Kneller, Y. Qiu, P. L. Tregenna-Piggott, C. M. Brown, J. R. Copley and R. M. Dimeo, *J. Res. Natl. Inst. Stand. Technol.*, 2009, **114**, 341.
34 A. J. O'Malley and C. R. A. Catlow, in *Experimental Methods in the Physical Sciences*, ed. F.-A. Felix and L. P. David, Academic Press, 2017, vol. 49, pp. 349–401.
35 *D. S. Materials Studio 8.0*, 5005 Wateridge Vista Drive, San Diego, CA 92121 USA, 2014.
36 http://www.iza-structure.org/databases/.
37 H. Sun, *J. Phys. Chem. B*, 1998, **102**, 7338–7364.
38 G. Goret, B. Aoun and E. Pellegrini, *J. Chem. Inf. Model.*, 2017, **57**, 1–5.
39 F. Volino and A. Dianoux, *Mol. Phys.*, 1980, **41**, 271–279.
40 M. Bee, *Biology and Materials Science*, Adam Hilger, Bristol, 1988, 193.
41 S. Gautam and D. Cole, *Chem. Phys.*, 2015, **458**, 68–76.
42 C. Chudley and R. Elliott, *Proc. Phys. Soc.*, 1961, **77**, 353.
43 A. R. Teixeira, X. Qi, C.-C. Chang, W. Fan, W. C. Conner and P. J. Dauenhauer, *J. Phys. Chem. C*, 2014, **118**, 22166–22180.